Research Paper

Effects of calcination and acid treatment on improving benzene adsorption performance of halloysite

Liangliang Deng[a,b], Peng Yuan[a,b,*], Dong Liu[a,b], Peixin Du[a,b], Junming Zhou[a,b], Yanfu Wei[c], Yaran Song[a,b], Yaqi Liu[a,b]

[a] CAS Key Laboratory of Mineralogy and Metallogeny, Guangdong Provincial Key Laboratory of Mineral Physics and Materials, Guangzhou Institute of Geochemistry, Institutions of Earth Science, Chinese Academy of Sciences, Guangzhou 510640, China
[b] University of Chinese Academy of Sciences, Beijing 100049, China
[c] Key Laboratory of Theoretical Chemistry of Environment, Ministry of Education, School of Chemistry and Environment, South China Normal University, Guangzhou 510006, China

ARTICLE INFO

ABSTRACT

In this paper, calcination and subsequent acid treatment were performed on halloysite to investigate their effects on dynamic benzene adsorption performance. Calcination at 800 °C had little effect on halloysite's tubular morphology, but it caused dehydroxylation and phase separation of amorphous SiO_2 and Al_2O_3. The occurrence of dehydroxylation resulted in removal of hydroxyl groups, which reduced halloysite's hydrophilicity, leading to an improvement in the halloysite's affinity for hydrophobic benzene molecules. The dynamic benzene adsorption capacity increased from 68.1 mg/g in the original halloysite to 103.6 mg/g in the calcined halloysite. The acid treatment after pre-calcination preserved the halloysite's tubular morphology and introduced massive micropores as a result of the rapid dissolution of Al_2O_3 layers. The emergence of these massive micropores substantially improved the specific surface area and dynamic benzene adsorption capacity of the acid-treated calcined halloysite, which reached 472.3 m^2/g and 204.2 mg/g, respectively. In addition, the recycling efficiency of the acid-treated calcined halloysite for benzene adsorption reached 92.5%, thus displaying good regeneration performance. These results demonstrate that calcination and subsequent acid treatment play important roles in promoting the halloysite's benzene adsorption performance, which makes the resulting halloysite a promising adsorbent for the treatment of volatile organic compounds.

1. Introduction

Volatile organic compounds (VOC) are the most common air pollutants emitted by the petrochemical, chemical, pharmaceutical, and printing industries and have attracted enormous attention in the field of environmental treatment due to their toxicity, harmfulness, and even carcinogenicity. In addition, VOC are the main sources of photochemical reactions that can trigger the formation of secondary organic aerosols, which are harmful to human health (Pöschl, 2005; Kroll and Seinfeld, 2008; Hallquist et al., 2009). Many technologies have been proposed for VOC control, including membrane separation (Belaissaoui et al., 2016), oxidation (Kamal et al., 2016), catalysis (Zhong et al., 2014), biological treatment (Doble, 2006), and adsorption (Yu et al., 2015a; Yuan et al., 2015b), which is the most applicable technology because of its low cost, low energy, and flexible systems (Yu et al., 2015b).

Adsorbents have great importance in the application of adsorption technology. Among the most commonly used adsorbents, activated carbon is the most versatile, owing to its low cost and excellent adsorption capacity (Liu et al., 2012). However, its utility is restricted by drawbacks such as fire risk, pore clogging, and regeneration difficulties (Zhao et al., 1998). Compared with activated carbon, synthetic zeolites, such as SBA-15 (Serrano et al., 2004; Hu et al., 2009) and ZSM-5 (Serrano et al., 2007), have the advantages of a controllable pore size and good chemical stability for VOC adsorption. However, the process of synthesizing zeolites is complex and costly (Cundy and Cox, 2005), which hinders their wide application. Therefore, the development of inexpensive adsorbents with good adsorption performance and desirable thermal stability has attracted great interest. Raw clay minerals have been proposed as alternative adsorbents due to their special

porous structure, excellent heat resistance, and low cost (Deng et al., 2017).

Halloysite is a naturally occurring 1:1 clay mineral, and it has a unique tubular morphology with a porous structure, including a one-dimensional cylindrical lumen in the mesopore size range (2–50 nm) and macropores (> 50 nm) derived from the inner cavity of the tubular halloysite particles (Lvov et al., 2008; Tan et al., 2013; Yuan et al., 2015a). The formation of halloysite's tubular morphology results from the wrapping of halloysite layers, which is driven by a mismatch between the oxygen-sharing tetrahedral SiO_4 sheet and the adjacent octahedral AlO_6 sheet in the 1:1 layer under favorable crystallization conditions and geological occurrences (Singh and Mackinnon, 1996; Tan et al., 2014). Generally, the tubular halloysite is 0.02–30 μm long, and its external and internal diameters are 30–190 nm and 10–100 nm, respectively (Yuan et al., 2008, 2013). In addition to its porous structure, tubular halloysite also possesses special surface properties of different internal and external surface groups. Its internal surface is composed of a gibbsite-like array of aluminol (Al−OH) groups, whereas the external surface consists of siloxane (Si−O−Si) groups (Yuan et al., 2008).

Because of its porous structure and special surface properties, halloysite is widely used as an adsorbent to remove aqueous pollutants, such as heavy metal ions (Kiani, 2014), phosphate (Wei et al., 2019), dyes (Peng et al., 2010), and antibiotics (Guan et al., 2012). However, the VOC adsorption performance of halloysite has rarely been studied. Deng et al. (2017) investigated the effects of the microstructure of montmorillonite and halloysite on their benzene adsorption performance and found that halloysite had a lower benzene adsorption capacity than montmorillonite because of its relatively smaller specific surface area (S_{BET}) and its lack of valid interlayer micropores for benzene adsorption. In the field of VOC adsorption, adsorbents with large S_{BET} and abundant micropores usually display good adsorption performance (Dou et al., 2011). Therefore, adjusting the surface properties and structure of halloysite might be an effective way to improve its VOC adsorption performance.

Several methods have been suggested to adjust the surface properties and structure of halloysite, including silylation (Yuan et al., 2008), intercalation (Mellouk et al., 2009), calcination (Yuan et al., 2012), and acid treatment (Abdullayev et al., 2012; Gaaz et al., 2016); among these, calcination and acid treatment are relatively easier to conduct. Calcination can lead to dehydration, dehydroxylation, and phase transition and cause distortion and destruction of the tubular structure (Yuan et al., 2012). Acid treatment has been regarded as an effective method to enhance the S_{BET} of halloysite (Fu et al., 2017); however, the S_{BET} of halloysite after directly acid-treated treatment was restricted at around 250 m²/g (Shu et al., 2015). It was reported that the S_{BET} of halloysite could be further improved via calcination before acid treatment (Belkassa et al., 2013); however, the VOC adsorption performance of acid-treated calcined halloysite has not been reported, and the related mechanisms remain unclear.

In this study, calcined halloysite and acid-treated calcined halloysite were prepared. X-ray diffraction (XRD), Fourier-transform infrared (FTIR) spectroscopy, transmission electron microscopy (TEM), and N_2 adsorption-desorption were used to characterize the structure of the calcined halloysite and the acid-treated calcined halloysite. Benzene, a commonly used solvent in industrial processes that ranks at the top of the list of VOC pollutants, was selected as a model organic pollutant to investigate the effects of calcination and the subsequent acid treatment on the VOC adsorption performance of halloysite via a breakthrough curve method.

2. Experiment

2.1. Regents and materials

Analytical grade sulphuric acid was provided by Guangzhou

Chemical Reagent Co., Ltd. Sodium hexametaphosphate (AR grade) was purchased from Guangzhou Chemical Reagent Co., Ltd. Distilled water was used in all experiments. The raw halloysite sample, obtained from Linfen, Shanxi Province, China, was purified by hand-picking and the following sedimentation (Tan et al., 2013). A typical purification procedure was briefly described as follows: (1) The raw halloysite sample was smashed, and the white fragments were selected. (2) The selected white fragments were ground and then added to the distilled water with a solid-liquid ratio of 3 g: 100 mL. (3) 1.0 mass% sodium hexametaphosphate was added to the dispersion under stirring, serving as a dispersant. (4) The dispersion was stirred for 30 min and left to stand for 25 h (calculated by Stokes law) at room temperature. (5) The < 2 μm fraction was collected from the dispersion by siphon and dried overnight at 120 °C, obtaining the purified halloysite (hereafter denoted as Hal). The chemical composition (mass%) of Hal was as follows: SiO_2, 41.05; Al_2O_3, 34.97; Fe_2O_3, 0.30; MgO, 0.16; K_2O, 0.06; CaO, 0.23; Na_2O, 0.25; MnO, 0.03; TiO_2, 0.14; and ignition loss, 22.76.

2.2. Preparation of calcined halloysite and acid-treated calcined halloysite

Hal was first calcined in a programmed temperature-controlled muffle furnace at 800 °C for 3 h and denoted $Hal_{800°C}$. Then, 2.0 g of $Hal_{800°C}$ was mixed with 80 mL of 3 M H_2SO_4 solution in a sealed glass vessel, and the dispersion was stirred vigorously in a water bath at 80 °C for 2 h, 4 h, and 8 h, respectively. Finally, the solid in mixture was separated via centrifugation, washed repeatedly with distilled water until it reached a neutral pH, and dried overnight at 120 °C. The acid-treated calcined halloysite was labeled $Hal_{800°C}$-ATx, where x was the acid treatment time. For example, $Hal_{800°C}$-AT2 refers to the halloysite that was pre-calcined at 800 °C and then acid-treated for 2 h.

2.3. Characterization methods

Major element oxides were analyzed on fused glass beads with a Rigaku RIX 2000 X-ray fluorescence spectrometer. To determine loss on ignition, 1000 mg of sample powder was heated to 1000 °C and maintained there for 10 min.

The XRD patterns were recorded with a Bruker D8 Advance diffractometer with a Ni filter and Cu-Kα radiation (λ = 0.154 nm) using a generator voltage of 40 kV and a current of 40 mA. The scan rate was 3° (2θ)/min.

N_2 adsorption-desorption isotherms were measured with a Micromeritics ASAP2020 system at liquid-nitrogen temperature. The samples were outgassed at 120 °C for 12 h before measurements were made. The samples' S_{BET} values were calculated from the nitrogen adsorption data using the multiple-point Brunauer-Emmett-Teller (BET) method (Brunauer et al., 1938), and the total pore volume (V_{total}) was estimated based on the nitrogen uptake at a relative pressure of approximately 0.97. The samples' microporous surface area (S_{micro}) and microporous volume (V_{micro}) were derived with the t-plot method. The non-local density functional theory (NLDFT) model (Thommes et al., 2015) was used to determine the samples' micropore and mesopore size distributions.

TEM and energy dispersive spectroscopy (EDS) were performed with an FEI Talos F200S field-emission transmission electron microscope operating at an accelerating voltage of 200 kV. The specimens for TEM observation were prepared with the following procedure. The sample was ultrasonically dispersed in ethanol for 5 min, and a drop of sample dispersion was dropped onto a carbon-coated copper grid, which was left to stand for 10 min and transferred to the microscope.

FTIR spectra were recorded with a Bruker Vertex 70 IR spectrometer. The specimens used for FTIR measurement were prepared by mixing 0.9 mg of sample powder with 80.0 mg of KBr and pressing the mixture into a pellet. For each FTIR measurement, 64 scans were collected over the range of 400 to 4000 cm^{-1} at a resolution of 4 cm^{-1}.
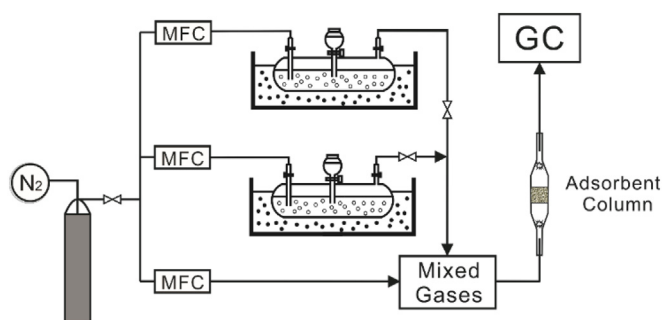
Fig. 1. Schematic diagram of experimental set-up (MFC: mass flow controller).

2.4. Benzene adsorption test

The samples' benzene adsorption performance was evaluated with an in-line gas chromatography apparatus (Fig. 1). Before adsorption, the samples were heated at 120 °C in a muffle oven for 2 h, which removed most of the physically adsorbed water molecules and small organic impurities adsorbed in the pores. During the adsorption measurement, the organic saturator with benzene was immersed in a water bath at 30 °C. Each powder sample was weighed at approximately 0.5 g and loaded into a glass column. The column was fed with a dry nitrogen stream containing benzene vapor at 3.00 mL/min, which was adjustable with a mass flow controller (MFC). The concentrations of benzene in both the column influent and effluent were quantified with a gas chromatograph (Agilent 7820A) with a flame ionization detector. The experiment was ended when the adsorption equilibrium was reached. After adsorption, the glass column with the sample was heated at 120 °C for 12 h for desorption of the adsorbed benzene molecules and then retested. This process was repeated five times to evaluate the sample's regeneration performance.

The adsorbents' benzene adsorption capacity (q, mg/g) was calculated by integrating the area above the acquired breakthrough curve after subtracting the area attributed to the system dead volume, according to the following equation:

$$q = \frac{M}{1000m} \int_{t_1}^{t_2} F[C_0 - C_t] dt \qquad (1)$$

where M (g/mol) is the molecular mass of benzene; m (g) is the initial mass of the adsorbents before testing; t_1 (min) is the breakthrough time without the samples; t_2 (min) is the breakthrough time with the packed column; C_0 and C_t (mmol/L) represent the influent and measured effluent benzene concentrations, respectively; and F (mL/min) is the N_2 flow rate. The dead space was determined by performing blank runs without the column.

The breakthrough curves were fitted using Yoon and Nelson model (Yoon and Nelson, 1984).

$$t = \tau + \frac{1}{k} \ln \frac{C_t}{C_0 - C_t} \qquad (2)$$

where t (min) is the breakthrough time; C_t and C_0 are the outlet and inlet concentrations of the stream through the adsorbent column, respectively; τ (min) is the time at which the breakthrough concentration reached half the initial concentration ($C_t = 0.5 \, C_0$); and k is a mass transfer coefficient.

3. Results and discussion

3.1. Structure of calcined halloysite and acid-treated calcined halloysite

Fig. 2a presents the XRD patterns of Hal, $Hal_{800°C}$, and $Hal_{800°C}$-AT2. All the reflections in the XRD pattern of Hal were consistent with the characteristic reflections of halloysite (7 Å) with a d_{001} of 7.4 Å (Joussein et al., 2005), which indicated that Hal could be ascribed to

the dehydrated form of halloysite. After calcination at 800 °C, the reflections assigned to halloysite (7 Å) disappeared from the XRD pattern of $Hal_{800°C}$ (Fig. 2a), but a broad reflection with a center at around 3.8 Å emerged. This change was attributed to the formation of amorphous metahalloysite by calcination (Kadi et al., 2012; Yuan et al., 2012). Compared to $Hal_{800°C}$, the center of the broad reflection on the XRD pattern of $Hal_{800°C}$-AT2 (Fig. 2a) shifted slightly, from 3.8 Å to 4.1 Å, which was in accordance with the characteristic reflection of amorphous SiO_2 (Martínez et al., 2006), thus implying a transformation from amorphous metahalloysite to amorphous SiO_2. This transformation might occur due to the dissolution of Al_2O_3, resulting from the phase separation of amorphous SiO_2 and Al_2O_3 in metahalloysite (Yuan et al., 2012), which could be verified by the FTIR spectra (Fig. 2b). In addition, the intensity of the broad reflection on the XRD pattern of $Hal_{800°C}$-AT2 was stronger than that on the XRD pattern of $Hal_{800°C}$ due to the increase in the relative content of amorphous SiO_2 after the dissolution of Al_2O_3. The XRD patterns of $Hal_{800°C}$-AT4 and $Hal_{800°C}$-AT8 are not shown in Fig. 2a because they are similar to that of $Hal_{800°C}$-AT2, which suggests the maintenance of amorphous SiO_2 in the acid-treatment process.

The FTIR spectra of Hal, $Hal_{800°C}$, and $Hal_{800°C}$-AT2 are displayed in Fig. 2b, and the position and assignment of each vibration are listed in Table 1, which are based on previous reports on halloysite, alumina, and silica (Dablemont et al., 2008; Al-Oweini and El-Rassy, 2009; Yuan et al., 2012, 2016). Two bands centered at 3696 and 3623 cm^{-1} were present in the hydroxyl region (3000–4000 cm^{-1}) of the spectrum of Hal (Fig. 2b) and were ascribed to the O−H stretching of inner-surface hydroxyl groups and inner hydroxyl groups, respectively. In addition, a broad band centered at 3436 cm^{-1} and a weak one at 1630 cm^{-1} also appeared and were assigned to the O−H stretching and O−H deformation of physically adsorbed water, respectively. The bands at 1090 and 1033 cm^{-1} corresponded to the in-plane Si−O stretching vibration. The band at 911 cm^{-1} was ascribed to O−H deformation of inner hydroxyl groups, and that at 793 cm^{-1} was caused by symmetric stretching of Si−O. The bands at 754 and 691 cm^{-1} were attributed to perpendicular Si−O stretching. The three remaining bands at 536, 469, and 437 cm^{-1} were caused by the deformation of Al−O−Si, Si−O−Si, and Si−O, respectively. Compared with the spectrum of Hal (Fig. 2b), the O−H stretching bands of the inner-surface hydroxyl groups (3696 cm^{-1}) and inner hydroxyl groups (3623 cm^{-1}), and the O−H deformation band of the inner hydroxyl groups (911 cm^{-1}) disappeared from the spectrum of $Hal_{800°C}$ (Fig. 2b), implying the dehydroxylation of Hal after calcination at 800 °C. Moreover, the absence of the bands of Si−O framework (1033, 793, 754, 691, and 437 cm^{-1}) and the deformation vibrations of Al−O−Si (536 cm^{-1}) suggested the breakdown of the ordered Si_2O_5 network and the separation of the silica and alumina originally present in the tetrahedral and octahedral sheets, respectively. These results are in accordance with those of previous studies on the changes in the structure of halloysite during heating, which revealed the transformation of halloysite to metahalloysite at calcination temperature between 500 °C and 900 °C and the phase separation of amorphous SiO_2 and Al_2O_3 in metahalloysite (Yuan et al., 2012). The presence of the ^{VI}Al−O stretching band at 814 cm^{-1} confirmed the formation of Al_2O_3. After 2 h of acid treatment, the ^{VI}Al−O stretching band at 814 cm^{-1} vanished from the spectrum of $Hal_{800°C}$-AT2 (Fig. 2b), indicating the absolute removal of Al_2O_3. In addition, the emergence of the bending bands of Si−OH and Si−O−Si, centered at 949 and 800 cm^{-1}, respectively, and the Si−O stretching bands of the SiO_2 network defects at 562 cm^{-1} (Al-Oweini and El-Rassy, 2009), implied that amorphous SiO_2 was preserved. This result was consistent with the XRD pattern of $Hal_{800°C}$-AT2 (Fig. 2a), which showed a characteristic reflection of amorphous SiO_2. Furthermore, the adsorbed water bands (3413 and 1630 cm^{-1}) on the FTIR spectrum of $Hal_{800°C}$-AT2 were much more intense than those of the FTIR spectrum of $Hal_{800°C}$, which suggests that $Hal_{800°C}$-AT2 was more hydrophilic than $Hal_{800°C}$ due to the hydroxylation of $Hal_{800°C}$-AT2 after acid treatment.
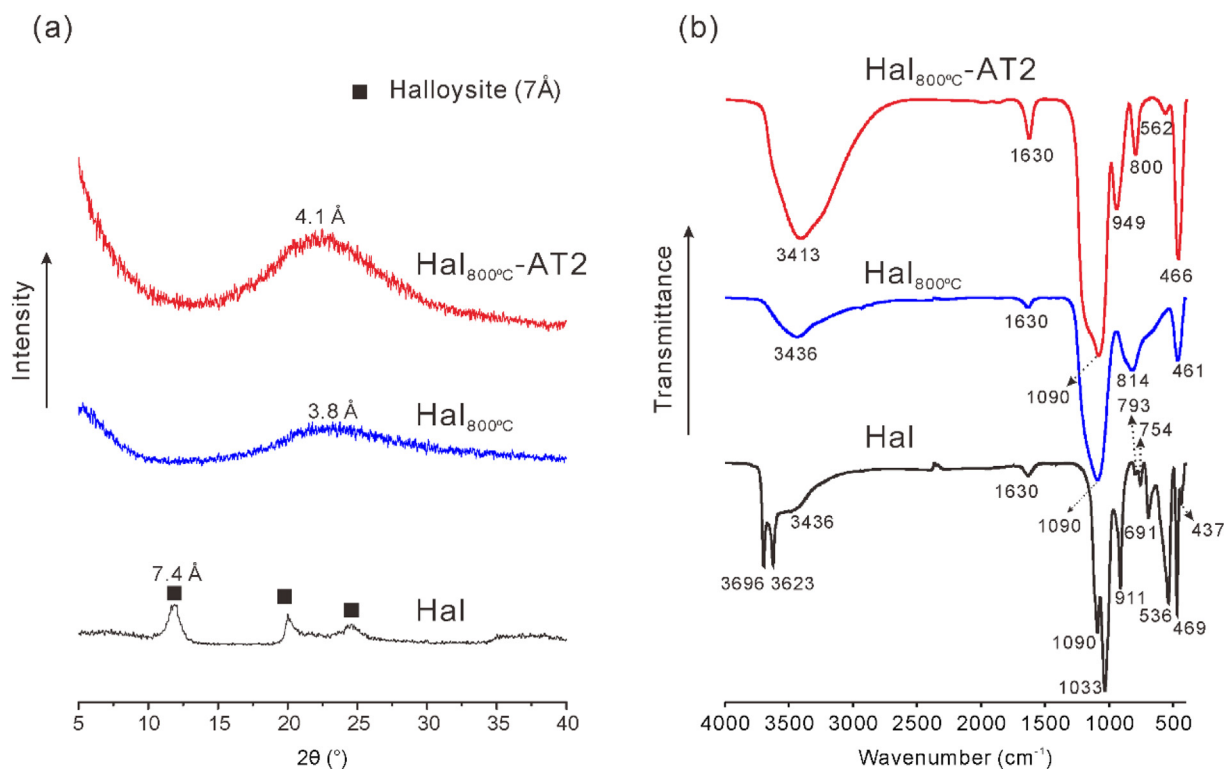
Fig. 2. XRD patterns (a) and FTIR spectra (b) of Hal, $Hal_{800°C}$, and $Hal_{800°C}$-AT2.

Table 1
Positions and assignments of FTIR vibration bands.

Position (cm^{-1})	Assignments
3696	O−H stretching of inner-surface hydroxyl groups
3623	O−H stretching of inner hydroxyl groups
3413/3436	O−H stretching of adsorbed water
1630	O−H deformation of adsorbed water
1090	In-plane Si−O stretching
1033	In-plane Si−O stretching
949	Deformation of Si−OH
911	O−H deformation of inner hydroxyl groups
814	Al−O vibration associated with six coordinated Al
800	Deformation of Si−O−Si
793	Symmetric stretching of Si−O
754	Perpendicular Si−O stretching
691	Perpendicular Si−O stretching
562	Si−O stretching
536	Deformation of Al−O−Si
461–469	Deformation of Si−O−Si
437	Deformation of Si−O

The FTIR spectra of $Hal_{800°C}$-AT4 and $Hal_{800°C}$-AT8 were similar to that of $Hal_{800°C}$-AT2, thus their FTIR spectra are not shown in Fig. 2b.

As shown in the TEM image of Hal in Fig. 3a, the morphology of halloysite particles is cylindrical with a transparent central area parallel to the cylinder, which implies that the particles are hollow and open-ended. The length of the halloysite ranges from 0.02 to 30.0 μm, and its external and internal diameters are 30–190 nm and 10–100 nm, respectively, as determined in a previous study (Yuan et al., 2008, 2013). The TEM image of $Hal_{800°C}$ (Fig. 3b) shows that the halloysite maintained its tubular morphology after calcination, which suggests that calcination at 800 °C had little effect on halloysite's tubular morphology. This result is in agreement with that of previous report, which demonstrated that the tubular morphology of halloysite could remain largely intact as heating temperature below 900 °C (Yuan et al., 2012). The TEM images of $Hal_{800°C}$-AT2, $Hal_{800°C}$-AT4, and $Hal_{800°C}$-AT8 (Fig. 3c-e) reveal that acid-treated calcined halloysite also preserved its

tubular morphology and had a relatively uniform lumen. However, the EDS data of $Hal_{800°C}$-AT2 (Fig. 3c) showed the absence of Al, thus indicating the complete removal of Al_2O_3. This result was in accordance with the disappearance of the ^{VI}Al−O stretching band on the FTIR spectrum of $Hal_{800°C}$-AT2 (Fig. 2b). In addition, some nanoparticles emerged in the lumen of $Hal_{800°C}$-AT4 and $Hal_{800°C}$-AT8 (Fig. 3d and e). These nanoparticles could be ascribed to silica nanoparticles originating from the curving and aggregation of 2D silica nanosheets, owing to the disaggregation of amorphous SiO_2 layers after the dissolution of Al_2O_3 layers (Zhang et al., 2012a; Fu et al., 2017).

According to these observations on the structure of acid-treated calcined halloysite ($Hal_{800°C}$-AT2, $Hal_{800°C}$-AT4 and $Hal_{800°C}$-AT8) and previous reports on the structure of halloysite after direct acid treatment (Abdullayev et al., 2012; Zhang et al., 2012b; Fu et al., 2017), pre-calcination has a significant effect on halloysite's acid-treating behavior. For the directly acid-treated halloysite, the acid treatment reaction was strongly affected by the reaction temperature, which caused the lumen to assume different shapes. When the reaction temperature exceeded 70 °C, the reaction was relatively intense and mainly took place from the tube end to the middle, resulting in a non-uniform lumen that was wider nearer the tube end and narrower in the middle. If the reaction temperature was lower than 70 °C, the acid treatment reaction was relatively mild, and it predominantly occurred from the inner octahedral layer to the outer one. The halloysite that underwent direct acid treatment below 70 °C possessed a uniform lumen due to the stripping of alumosilicate sheets layer by layer. In addition, a relatively long time was generally needed for complete dealumination of the directly acid-treated halloysite (i.e., several hours or days). However, the acid-treated calcined halloysite in this study not only maintained its tubular morphology, but it also showed a uniform lumen even though the acid treatment was performed above 70 °C, reaching 80 °C. Moreover, the Al_2O_3 layers in the acid-treated calcined halloysite were entirely removed within 2 h, which is a relatively short time. These results might be attributed to the phase separation of amorphous SiO_2 and Al_2O_3 resulting from calcination; this could have made it much easier to dissolve the Al_2O_3 than to break down the Al−O−Si network in the acid
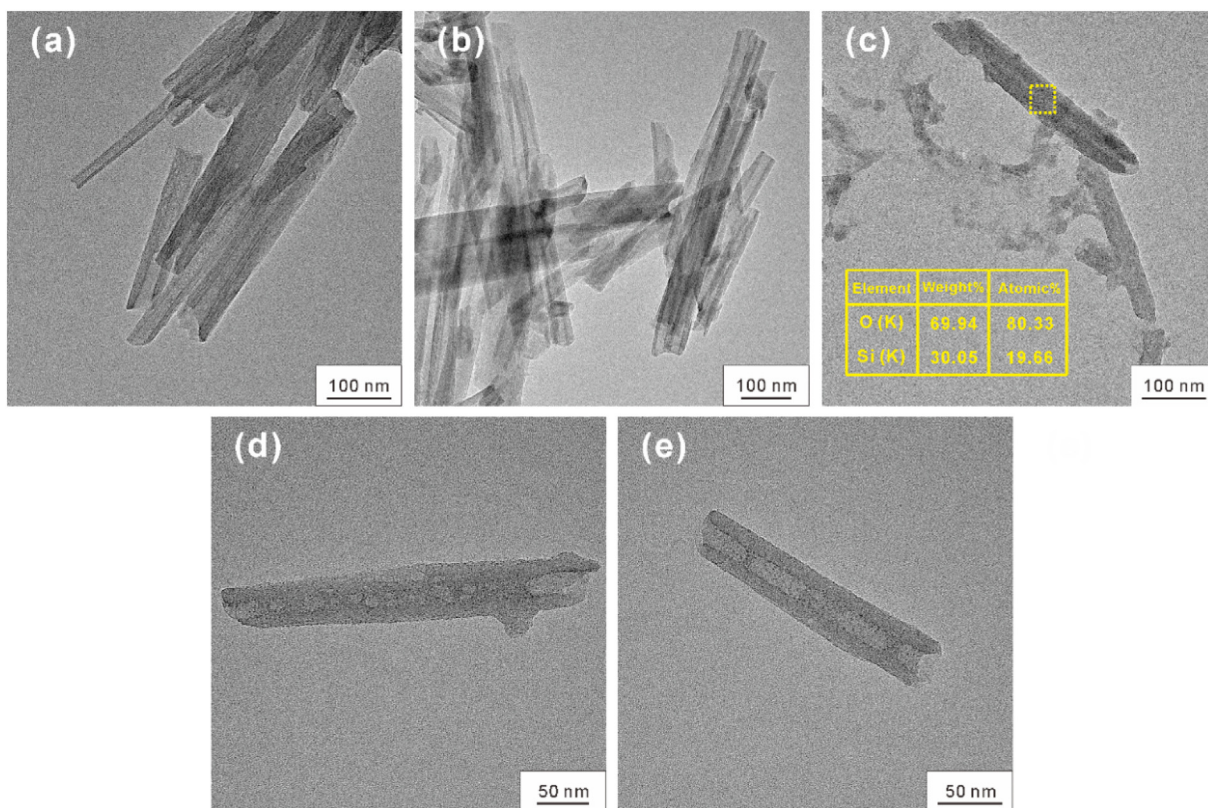
Fig. 3. TEM images of Hal (a), Hal$_{800°C}$ (b), Hal$_{800°C}$-AT2 (c), Hal$_{800°C}$-AT4 (d), and Hal$_{800°C}$-AT8 (e).

treatment process. Therefore, it can be assumed that all Al$_2$O$_3$ layers in the calcined halloysite were dissolved rapidly and almost simultaneously from the tube end to the middle rather than layer by layer in the acid treatment process, leading to the maintenance of the tubular morphology.

The N$_2$ adsorption-desorption isotherms of Hal, Hal$_{800°C}$, Hal$_{800°C}$-AT2, Hal$_{800°C}$-AT4, and Hal$_{800°C}$-AT8 are shown in Fig. 4a. According to the IUPAC classification refined by Thommes et al. (2015), the isotherm of Hal (Fig. 4a) was classified as type IV isotherms with an H3 hysteresis loop. The hysteresis in the isotherm is associated with filling via capillary condensation and emptying of mesopores, which stemmed primarily from the mesoscopic lumen. The sharp increase in the quantity of adsorbed N$_2$ near the relative pressure of one ($P/P_0 \approx 1$) corresponded to adsorption by macropores, resulting from the stacking of the aggregates of halloysite particles. Hal$_{800°C}$ showed an isotherm similar to Hal (Fig. 4a), indicating the limited influence of calcination at 800 °C

on the porous structure of Hal. The isotherms of Hal$_{800°C}$-AT2, Hal$_{800°C}$-AT4, and Hal$_{800°C}$-AT8 (Fig. 4a) were identical and could be characterized as type IV with an H3 hysteresis loop. The hysteresis loop was attributed to the preserved mesoscopic lumen, which was revealed on their TEM images (Fig. 3c-e) and later proven by their pore size distribution (PSD) curves (Fig. 4b). Compared to Hal and Hal$_{800°C}$, the isotherms of Hal$_{800°C}$-AT2, Hal$_{800°C}$-AT4, and Hal$_{800°C}$-AT8 (Fig. 4a) increased rapidly at a relatively low pressure ($P/P_0 < 0.1$), thus suggesting the presence of massive micropores. These micropores might be newly-formed due to the dissolution of Al$_2$O$_3$ layers and/or the stacking of the silica nanoparticles in the lumen, which were observed in the TEM images of Hal$_{800°C}$-AT4 and Hal$_{800°C}$-AT8 (Fig. 3d and e). In the relatively high-pressure region ($P/P_0 \approx 1$), the sharp increase of the isotherms of Hal$_{800°C}$-AT2, Hal$_{800°C}$-AT4, and Hal$_{800°C}$-AT8 implied the existence of macropores, owing to the stacking of the aggregates of particles.
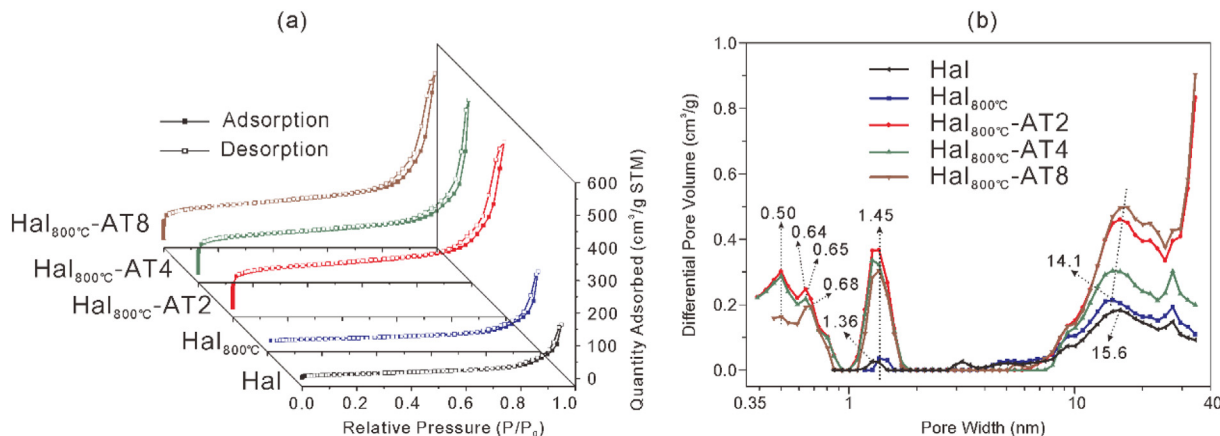

Fig. 4. N$_2$ adsorption-desorption isotherms (a) and NLDFT PSD curves (b) of Hal, Hal$_{800°C}$, Hal$_{800°C}$-AT2, Hal$_{800°C}$-AT4, and Hal$_{800°C}$-AT8.

Fig. 4b displays the NLDFT PSD curves of Hal, $Hal_{800°C}$, $Hal_{800°C}$-AT2, $Hal_{800°C}$-AT4, and $Hal_{800°C}$-AT8. The PSD curve of Hal (Fig. 4b) exhibited a minor micropore distribution and a primary mesopore distribution, with pore widths in the ranges of 1.2–1.6 and 10–20 nm, respectively. The micropores might be ascribed to the slit-shaped pores due to dehydration (Deng et al., 2017), and the mesopores corresponded to the mesoscopic lumen. $Hal_{800°C}$ showed a PSD curve similar to that of Hal; however, compared with the PSD curve of Hal, the centers of the micropore distribution and mesopore distribution on the PSD curve of $Hal_{800°C}$ shifted from 1.36 and 15.6 nm to 1.45 and 14.1 nm, respectively, indicating an increase in the pore size of the slit-shaped pores and a decrease in the diameter of the mesoscopic lumen. These changes could be attributed to the separation of amorphous SiO_2 layers and Al_2O_3 layers by calcination. After acid treatment, the PSD curves of $Hal_{800°C}$-AT2, $Hal_{800°C}$-AT4, and $Hal_{800°C}$-AT8 (Fig. 4b) showed a distinct micropore distribution at 1.45 nm, which was assigned to the slit-shaped pores resulting from dehydration. This result was due to the dissolution of Al_2O_3 layers, which allowed the nitrogen molecules to fully penetrate the slit-shaped pores. Moreover, the mesopore distribution, corresponding to the mesoscopic lumen, was also displayed on the PSD curves of $Hal_{800°C}$-AT2, $Hal_{800°C}$-AT4, and $Hal_{800°C}$-AT8 (Fig. 4b), which indicated the maintenance of the mesoscopic lumen. This result was consistent with the observation of the TEM images of $Hal_{800°C}$-AT2, $Hal_{800°C}$-AT4, and $Hal_{800°C}$-AT8 (Fig. 3c-e). However, compared to $Hal_{800°C}$, the mesopore distribution centers of $Hal_{800°C}$-AT2, $Hal_{800°C}$-AT4, and $Hal_{800°C}$-AT8 shifted toward the large pore width, which implied an increase in the diameter of the mesoscopic lumen. The enlargement of the mesoscopic lumen could be attributed to the dissolution of Al_2O_3 layers and the disaggregation of amorphous SiO_2 layers. In addition to the pore distributions of the slit-shaped pores and the mesoscopic lumen, two new micropore distributions emerged on the PSD curves of $Hal_{800°C}$-AT2, $Hal_{800°C}$-AT4, and $Hal_{800°C}$-AT8 relative to that of $Hal_{800°C}$, of which the pore centers were at around 0.50 and 0.64 nm, respectively. The thickness of the AlO_6 octahedral layer in halloysite is approximately 0.48 nm, which is close to 0.50 nm. Therefore, micropores with the diameter of 0.50 nm might be considered as originating from the dissolution of the Al_2O_3 layers. The formation of micropores with the pore size of 0.64 nm might result from the expansion of the micropores with a diameter of 0.50 nm, owing to peeling or disaggregation of the amorphous SiO_2 layers during the acid treatment process (Zhang et al., 2012a; Fu et al., 2017). This expansion became pronounced as the acid treatment time increased, which can be confirmed by the further migration of the pore center from 0.64 nm to 0.65 and 0.68 nm, as presented in the PSD curves of $Hal_{800°C}$-AT4 and $Hal_{800°C}$-AT8 (Fig. 4b).

The porous parameters are displayed in Table 2; the S_{BET} of Hal (58.4 m²/g) was slightly larger than that of $Hal_{800°C}$ (54.4 m²/g). The slight decrease in the S_{BET} of $Hal_{800°C}$ might be due to partial distortion of the tubular nanoparticles after calcination at 800 °C, although it often occurred at 1000 °C or even higher (Yuan et al., 2012). Compared to $Hal_{800°C}$, the S_{BET} of $Hal_{800°C}$-AT2 significantly increased to 472.3 m²/g (Table 2), and its S_{micro} reached 311.2 m²/g (Table 2), which indicates that the dominant porosity of $Hal_{800°C}$-AT2 was

micropores. The micropores of $Hal_{800°C}$-AT2 were formed by the dissolution of Al_2O_3 layers and by the exposure of the slit-shaped pores, as revealed by the PSD curve (Fig. 4b). As the acid treatment time increased, the S_{BET} of $Hal_{800°C}$-AT4 and $Hal_{800°C}$-AT8 (442.8 and 368.9 m²/g, respectively; Table 2) decreased relative to that of $Hal_{800°C}$-AT2 (472.3 m²/g; Table 2). This decrease in S_{BET} could be attributed to the disaggregation of amorphous SiO_2 layers and the diffusion of silica nanoparticles from the lumen to the outside of the tube (Zhang et al., 2012a; Fu et al., 2017). However, the S_{micro} of $Hal_{800°C}$-AT4 and $Hal_{800°C}$-AT8 still reached 287.2 and 210.1 m²/g, respectively (Table 2), which indicates the existence of substantial micropores. On the basis of the observation of the TEM images (Fig. 3d and e) and the analysis of the PSD curves (Fig. 4b), the formation of the micropores of $Hal_{800°C}$-AT4 and $Hal_{800°C}$-AT8 could be attributed to the dissolution of Al_2O_3 layers, the exposure of the slit-shaped pores, and/or the stacking of silica nanoparticles in the lumen.

3.2. Benzene adsorption performance of calcined halloysite and acid-treated calcined halloysite and its related mechanisms

Breakthrough measurement is regarded as a method of evaluating the dynamic adsorption performances of the adsorbents in a continuous VOC adsorption process. The breakthrough curves of all samples are shown in Fig. 5, and the dynamic adsorption capacities (q, mg/g) are listed in Table 3. Hal had the lowest q value of all samples (only 68.1 mg/g; Table 3) because its slit-shaped pores, generated by dehydration, were inaccessible to benzene molecules, thus benzene adsorption occurred mainly on the external surface, as reported previously (Deng et al., 2017). In addition, Hal has a relatively small S_{BET} (58.4 m²/g; Table 2), which represents relatively small amount of surface sites for adsorption. The q value of $Hal_{800°C}$ (103.6 mg/g; Table 3) was higher than that of Hal (68.1 mg/g; Table 3), even though $Hal_{800°C}$ had a smaller S_{BET} (54.4 m²/g; Table 2). This result indicates that the benzene adsorption capacities of Hal and calcined halloysite were not directly correlated with their S_{BET}. The improvement in the benzene adsorption performance of $Hal_{800°C}$ could be attributed to the removal of hydroxyl groups by dehydroxylation, because hydroxyl groups are hydrophilic and exhibit poor adsorption affinity for the hydrophobic benzene molecules (Yu et al., 2015c). This explanation could also be verified by the smaller k value of $Hal_{800°C}$ (0.108; Table 3) than Hal (0.241; Table 3). Generally, the k value represents the diffusion and mass transfer characteristics of an adsorbate in the adsorption process, and a small k value indicates the adsorbate's large diffusion and mass transfer difficulty. Therefore, the relatively smaller k value of $Hal_{800°C}$ indicated its greater affinity for benzene molecules owing to the
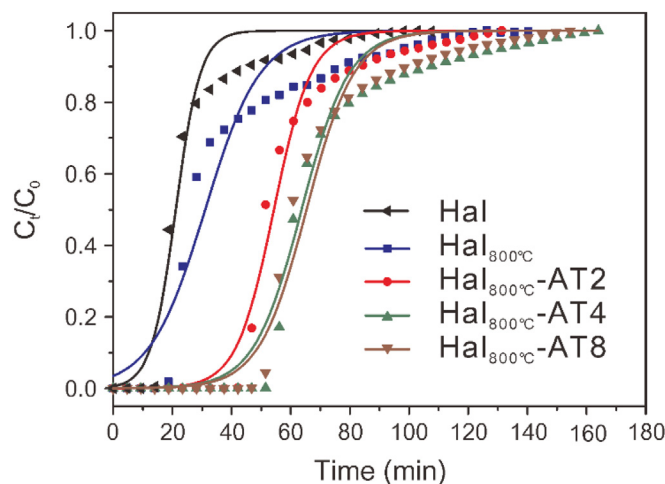
Table 2
Porous parameters of Hal, $Hal_{800°C}$, $Hal_{800°C}$-AT2, $Hal_{800°C}$-AT4, and $Hal_{800°C}$-AT8.

Samples	S_{BET} (m²/g)	S_{micro}^{a} (m²/g)	V_{total} (cm³/g)	V_{micro}^{a} (cm³/g)
Hal	58.4	–	0.270	–
$Hal_{800°C}$	54.4	–	0.202	–
$Hal_{800°C}$-AT2	472.3	311.2	0.668	0.126
$Hal_{800°C}$-AT4	442.8	287.2	0.584	0.116
$Hal_{800°C}$-AT8	368.9	210.1	0.684	0.086

[a] Microporous specific surface area and volume were calculated using the t-plot method.

Fig. 5. Breakthrough curves of Hal, $Hal_{800°C}$, $Hal_{800°C}$-AT2, $Hal_{800°C}$-AT4, and $Hal_{800°C}$-AT8.

Table 3

Dynamic adsorption capacity (*q*) and Yoon and Nelson equation parameters for benzene adsorption of Hal, $Hal_{800°C}$, $Hal_{800°C}$-AT2, $Hal_{800°C}$-AT4, and $Hal_{800°C}$-AT8.

Samples	q(mg/g)	τ(min)	k	R^2
Hal	68.1	21.2	0.241	0.964
$Hal_{800°C}$	103.6	31.1	0.108	0.937
$Hal_{800°C}$-AT2	166.3	54.3	0.159	0.980
$Hal_{800°C}$-AT4	204.2	65.3	0.125	0.974
$Hal_{800°C}$-AT8	195.7	63.7	0.126	0.980

removal of hydroxyl groups by calcination. The *q* value of $Hal_{800°C}$-AT2 reached 166.3 mg/g (Table 3), which was larger than that of $Hal_{800°C}$ (103.6 mg/g; Table 3). This result could be ascribed to the dissolution of Al_2O_3 layers by acid treatment, which introduced massive micropores and exposed the slit-shaped pores, thus providing much more adsorption space. However, relative to the significant improvement in S_{BET}, which increased from 54.4 m²/g of $Hal_{800°C}$ to 472.3 m²/g of $Hal_{800°C}$-AT2, the enhancement of the *q* value from 103.6 mg/g of $Hal_{800°C}$ to 166.3 mg/g of $Hal_{800°C}$-AT2 seemed relatively unequal. This result might be interpreted in the following way. Firstly, the increase in the S_{BET} and *q* values are both attributed to the appearance of micropores. However, the kinetic diameter of the nitrogen molecules (0.36 nm), used for S_{BET} measurement, was smaller than that of the benzene molecule (0.59 nm); the nitrogen molecules could thus penetrate the micropores much more easily than the benzene molecule, especially the micropores with a diameter of 0.50 nm, which might exhibit a sieving effect for benzene adsorption (Luebbers et al., 2010). Furthermore, $Hal_{800°C}$-AT2 was hydroxylated and more hydrophilic than $Hal_{800°C}$ after acid treatment, as confirmed by the FTIR spectra (Fig. 2b), so its surface might show a weaker affinity for benzene molecules than $Hal_{800°C}$, the dehydroxylated halloysite. Therefore, the benzene adsorption performance of halloysite and its derivates was affected not only by their structure but also by their surface properties. $Hal_{800°C}$-AT4 displayed the highest *q* value (204.2 mg/g; Table 3), even if its S_{BET} and S_{micro} (442.8 and 287.2 m²/g, respectively; Table 2) were smaller than those of $Hal_{800°C}$-AT2 (472.3 and 311.2 m²/g, respectively; Table 2). This result implies that not all micropores of the acid-treated calcined halloysite acted as adsorption sites for benzene molecules, possibly due to a sieving effect. The enhancement of the benzene adsorption capacity of $Hal_{800°C}$-AT4 (204.2 mg/g; Table 3) relative to that of $Hal_{800°C}$-AT2 (166.3 mg/g; Table 3) could be attributed to adsorption by the emerged silica nanoparticles in the lumen, as shown in the TEM image (Fig. 3d). The adsorption of silica nanoparticles for benzene molecules was confirmed by the decrease in the *k* value from 0.159 for $Hal_{800°C}$-AT2 to 0.125 for $Hal_{800°C}$-AT4 (Table 3), indicating the increase of diffuse and mass transfer difficulty of the adsorbed benzene molecules. With the acid treatment reaction proceeding, the emerged silica nanoparticles in the lumen diffused to the outside of the tube, leading to a decline in the benzene adsorption performance and the diffuse and mass transfer difficulty of adsorbed benzene molecules of the acid-treated calcined halloysite, whose *q* value decreased from 204.2 mg/g for $Hal_{800°C}$-AT4 to 195.7 mg/g for $Hal_{800°C}$-AT8, and the *k* value increased from 0.125 for $Hal_{800°C}$-AT4 to 0.126 for $Hal_{800°C}$-AT8.

Evaluation of the regeneration performance of VOC adsorbents is an important factor in their industrial application. The breakthrough process of benzene adsorption over $Hal_{800°C}$-AT4 was performed five times (Fig. 6), and the breakthrough curves of $Hal_{800°C}$-AT4 exhibited relatively good repeatability over five cycles of benzene adsorption. In addition, the recycling efficiency of $Hal_{800°C}$-AT4 after five cycles of benzene adsorption still reached 92.5% (Table 4), thus indicating good regeneration performance.

Raw clay minerals are regarded as potential adsorbents for VOC treatment. Studies have investigated the dynamic benzene adsorption performance of various clay minerals, including kaolinite (Kaol),
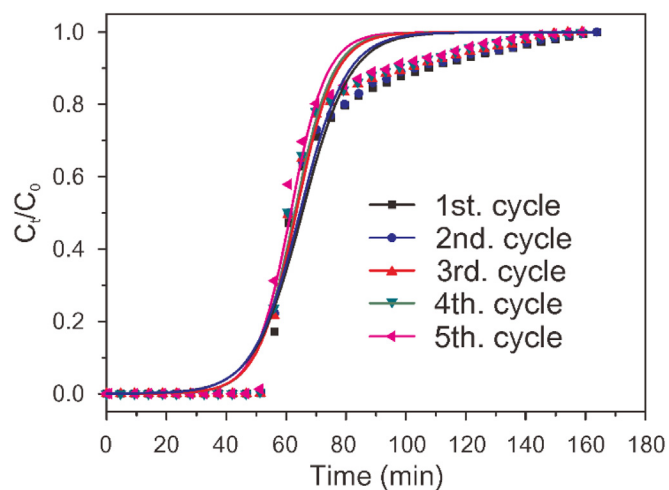

Fig. 6. Benzene adsorption breakthrough curves of $Hal_{800°C}$-AT4 cycled for five times.

Table 4

Dynamic adsorption capacity (*q*) and Yoon and Nelson equation parameters for various cycles of $Hal_{800°C}$-AT4.

Cycles	q (mg/g)	τ (min)	k	R^2	Efficiency (%)
First	204.2	65.3	0.125	0.974	–
Second	201.5	64.5	0.129	0.976	98.7%
Third	194.6	63.3	0.154	0.980	95.3%
Fourth	193.2	62.8	0.159	0.982	94.6%
Fifth	188.9	61.5	0.168	0.982	92.5%

montmorillonite (Mt), and allophane (Allo) (Deng et al., 2017, 2018). This study found that $Hal_{800°C}$-4 h exhibited substantially greater dynamic adsorption capacity than Kaol (56.7 mg/g), Mt. (141.2 mg/g), and Allo (105.9 mg/g). These results could be attributed to difference in structure. Kaol is short of micropores, and the benzene molecules were mainly adsorbed at the external surface. In addition, the S_{BET} of Kaol (17.9 m²/g) was very small, so its dynamic adsorption capacity (56.7 mg/g) was lower than that of $Hal_{800°C}$-AT4 (204.2 mg/g; Table 3). The interlayer micropores of Mt. could provide space for benzene adsorption, but its interlayer space is limited and is generally occupied by water molecules, so its dynamic adsorption capacity (141.2 mg/g) is relatively lower than that of $Hal_{800°C}$-AT4 (204.2 mg/g; Table 3). Allo also possesses substantial micropores, of which the S_{micro} reached 183.8 m²/g. However, compared to $Hal_{800°C}$-AT4, which has a relatively uniform tubular structure, the Allo nanoparticles showed severe aggregation, resulting in the formation of numerous pores with irregular and non-uniform channels, which are difficult for the benzene molecules to penetrate. Therefore, $Hal_{800°C}$-AT4 also showed better benzene adsorption performance than Allo. Moreover, compared to flammable activated carbon, $Hal_{800°C}$-AT4 could be ascribed to amorphous SiO_2, as displayed by the XRD pattern (Fig. 2a), which is incombustible and generally possesses good thermal stability. Therefore, $Hal_{800°C}$-AT4 might have great advantages in thermal regeneration relative to activated carbon.

4. Conclusion

In summary, calcination and the subsequent acid treatment promoted the dynamic benzene adsorption performance of halloysite. Calcination at 800 °C had little effect on halloysite's tubular morphology, but it improved halloysite's affinity for benzene molecules due to the occurrence of dehydroxylation. The acid treatment after precalcination not only maintained the halloysite's tubular morphology, it also introduced massive micropores by dissolving the Al_2O_3 layers,

resulting in significant enhancement of dynamic benzene adsorption capacity. In addition, the acid-treated calcined halloysite exhibited a high recycling efficiency for benzene adsorption and can be utilized as an effective VOC adsorbent. Calcination and the subsequent acid treatment might be an efficacious and practical method to enhance the VOC adsorption performance of clay minerals.

Acknowledgements

References

Abdullayev, E., Joshi, A., Wei, W., Zhao, Y., Lvov, Y., 2012. Enlargement of halloysite clay nanotube lumen by selective etching of aluminum oxide. ACS Nano 6, 7216–7226.

Al-Oweini, R., El-Rassy, H., 2009. Synthesis and characterization by FTIR spectroscopy of silica aerogels prepared using several Si(OR)$_4$ and R″Si(OR')$_3$ precursors. J. Mol. Struct. 919, 140–145.

Belaissaoui, B., Le Moullec, Y., Favre, E., 2016. Energy efficiency of a hybrid membrane/condensation process for VOC (volatile organic compounds) recovery from air: a generic approach. Energy 95, 291–302.

Belkassa, K., Bessaha, F., Marouf-Khelifa, K., Batonneau-Gener, I., Comparot, J.D., Khelifa, A., 2013. Physicochemical and adsorptive properties of a heat-treated and acid-leached Algerian halloysite. Colloid Surf. A 421, 26–33.

Brunauer, S., Emmett, P.H., Teller, E., 1938. Adsorption of gases in multimolecular layers. J. Am. Chem. Soc. 60, 309–319.

Cundy, C.S., Cox, P.A., 2005. The hydrothermal synthesis of zeolites: precursors, intermediates and reaction mechanism. Microporous Mesoporous Mater. 82, 1–78.

Dablemont, C., Lang, P., Mangeney, C., Piquemal, J.-Y., Petkov, V., Herbst, F., Viau, G., 2008. FTIR and XPS study of Pt nanoparticle functionalization and interaction with alumina. Langmuir 24, 5832–5841.

Deng, L., Yuan, P., Liu, D., Annabi-Bergaya, F., Zhou, J., Chen, F., Liu, Z., 2017. Effects of microstructure of clay minerals, montmorillonite, kaolinite and halloysite, on their benzene adsorption behaviors. Appl. Clay Sci. 143, 184–191.

Deng, L., Du, P., Yu, W., Yuan, P., Annabi-Bergaya, F., Liu, D., Zhou, J., 2018. Novel hierarchically porous allophane/diatomite nanocomposite for benzene adsorption. Appl. Clay Sci. 168, 155–163.

Doble, M., 2006. Biological treatment of VOCs. Chem. Eng. (N. Y.) 113, 35–41.

Dou, B., Hu, Q., Li, J., Qiao, S., Hao, Z., 2011. Adsorption performance of VOCs in ordered mesoporous silicas with different pore structures and surface chemistry. J. Hazard. Mater. 186, 1615–1624.

Fu, L., Yang, H., Tang, A., Hu, Y., 2017. Engineering a tubular mesoporous silica nanocontainer with well-preserved clay shell from natural halloysite. Nano Res. 10, 2782–2799.

Gaaz, T.S., Sulong, A.B., Aah, K., Nassir, M.H., Al-Amiery, A.A., 2016. Impact of sulfuric acid treatment of halloysite on physico-chemic property modification. Materials 9, 620.

Guan, W., Wang, X., Pan, J., Lei, J., Zhou, Y., Lu, C., Yan, Y., 2012. Synthesis of magnetic halloysite composites for the effective removal of tetracycline hydrochloride from aqueous solutions. Adsorpt. Sci. Technol. 30, 579–591.

Hallquist, M., Wenger, J., Baltensperger, U., Rudich, Y., Simpson, D., Claeys, M., Dommen, J., Donahue, N., George, C., Goldstein, A., 2009. The formation, properties and impact of secondary organic aerosol: current and emerging issues. Atmos. Chem. Phys. 9, 5155–5236.

Hu, Q., Li, J.J., Hao, Z.P., Li, L.D., Qiao, S.Z., 2009. Dynamic adsorption of volatile organic compounds on organofunctionalized SBA-15 materials. Chem. Eng. J. 149, 281–288.

Joussein, E., Petit, S., Churchman, J., Theng, B., Righi, D., Delvaux, B., 2005. Halloysite clay minerals—a review. Clay Miner. 40, 383–426.

Kadi, S., Lellou, S., Marouf-Khelifa, K., Schott, J., Gener-Batonneau, I., Khelifa, A., 2012. Preparation, characterisation and application of thermally treated Algerian halloysite. Microporous Mesoporous Mater. 158, 47–54.

Kamal, M.S., Razzak, S.A., Hossain, M.M., 2016. Catalytic oxidation of volatile organic compounds (VOCs)–a review. Atmos. Environ. 140, 117–134.

Kiani, G., 2014. High removal capacity of silver ions from aqueous solution onto halloysite nanotubes. Appl. Clay Sci. 90, 159–164.

Kroll, J.H., Seinfeld, J.H., 2008. Chemistry of secondary organic aerosol: formation and evolution of low-volatility organics in the atmosphere. Atmos. Environ. 42, 3593–3624.

Liu, D., Yuan, P., Tan, D., Liu, H., Wang, T., Fan, M., Zhu, J., He, H., 2012. Facile

preparation of hierarchically porous carbon using diatomite as both template and catalyst and methylene blue adsorption of carbon products. J. Colloid Interface Sci. 388, 176–184.

Luebbers, M.T., Wu, T., Shen, L., Masel, R.I., 2010. Effects of molecular sieving and electrostatic enhancement in the adsorption of organic compounds on the zeolitic imidazolate framework ZIF-8. Langmuir 26, 15625–15633.

Lvov, Y.M., Shchukin, D.G., Mohwald, H., Price, R.R., 2008. Halloysite clay nanotubes for controlled release of protective agents. ACS Nano 2, 814–820.

Martínez, J.R., Palomares-Sánchez, S., Ortega-Zarzosa, G., Ruiz, F., Chumakov, Y., 2006. Rietveld refinement of amorphous SiO$_2$ prepared via sol–gel method. Mater. Lett. 60, 3526–3529.

Mellouk, S., Cherifi, S., Sassi, M., Marouf-Khelifa, K., Bengueddach, A., Schott, J., Khelifa, A., 2009. Intercalation of halloysite from Djebel Debagh (Algeria) and adsorption of copper ions. Appl. Clay Sci. 44, 230–236.

Peng, L., Zhao, Y., Bing, Z., Liu, J., Yong, Y., Liu, J., 2010. Study on the adsorption of Neutral Red from aqueous solution onto halloysite nanotubes. Water Res. 44, 1489–1497.

Pöschl, U., 2005. Atmospheric aerosols: composition, transformation, climate and health effects. Angew. Chem. Int. Ed. 44, 7520–7540.

Serrano, D.P., Calleja, G., Botas, J.A., Gutierrez, F.J., 2004. Adsorption and hydrophobic properties of mesostructured MCM-41 and SBA-15 materials for volatile organic compound removal. Ind. Eng. Chem. Res. 43, 7010–7018.

Serrano, D.P., Calleja, G., Botas, J.A., Gutierrez, F.J., 2007. Characterization of adsorptive and hydrophobic properties of silicalite-1, ZSM-5, TS-1 and Beta zeolites by TPD techniques. Sep. Purif. Technol. 54, 1–9.

Shu, Z., Chen, Y., Zhou, J., Li, T., Yu, D., Wang, Y., 2015. Nanoporous-walled silica and alumina nanotubes derived from halloysite: controllable preparation and their dye adsorption applications. Appl. Clay Sci. 112–113, 17–24.

Singh, B., Mackinnon, I.D., 1996. Experimental transformation of kaolinite to halloysite. Clay Clay Miner. 44, 825–834.

Tan, D., Yuan, P., Annabi-Bergaya, F., Yu, H., Liu, D., Liu, H., He, H., 2013. Natural halloysite nanotubes as mesoporous carriers for the loading of ibuprofen. Microporous Mesoporous Mater. 179, 89–98.

Tan, D., Yuan, P., Annabi-Bergaya, F., Liu, D., Wang, L., Liu, H., He, H., 2014. Loading and in vitro release of ibuprofen in tubular halloysite. Appl. Clay Sci. 96, 50–55.

Thommes, M., Kaneko, K., Neimark, A.V., Olivier, J.P., Rodriguez-Reinoso, F., Rouquerol, J., Sing, K.S., 2015. Physisorption of gases, with special reference to the evaluation of surface area and pore size distribution (IUPAC Technical Report). Pure Appl. Chem. 87, 1051–1069.

Wei, Y., Yuan, P., Liu, D., Losic, D., Tan, D., Chen, F., Liu, H., Zhou, J., Du, P., Song, Y., 2019. Activation of natural halloysite nanotubes by introducing lanthanum oxycarbonate nanoparticles via co-calcination for outstanding phosphate removal. Chem. Commun. 55, 2110–2113.

Yoon, Y.H., Nelson, J.H., 1984. Application of gas adsorption kinetics I. A theoretical model for respirator cartridge service life. Am. Ind. Hyg. Assoc. J. 45, 509–516.

Yu, W., Deng, L., Yuan, P., Liu, D., Yuan, W., Chen, F., 2015a. Preparation of hierarchically porous diatomite/MFI-type zeolite composites and their performance for benzene adsorption: the effects of desilication. Chem. Eng. J. 270, 450–458.

Yu, W., Yuan, P., Liu, D., Deng, L., Yuan, W., Tao, B., Cheng, H., Chen, F., 2015b. Facile preparation of hierarchically porous diatomite/MFI-type zeolite composites and their performance of benzene adsorption: the effects of NaOH etching pretreatment. J. Hazard. Mater. 285, 173–181.

Yu, W., Deng, L., Yuan, P., Liu, D., Yuan, W., Liu, P., He, H., Li, Z., Chen, F., 2015c. Surface silylation of natural mesoporous/macroporous diatomite for adsorption of benzene. J. Colloid Interface Sci. 448, 545–552.

Yuan, P., Southon, P.D., Liu, Z., Green, M.E., Hook, J.M., Antill, S.J., Kepert, C.J., 2008. Functionalization of halloysite clay nanotubes by grafting with γ-aminopropyltriethoxysilane. J. Phys. Chem. C 112, 15742–15751.

Yuan, P., Tan, D., Annabi-Bergaya, F., Yan, W., Fan, M., Liu, D., He, H., 2012. Changes in structure, morphology, porosity, and surface activity of mesoporous halloysite nanotubes under heating. Clay Clay Miner. 60, 561–573.

Yuan, P., Tan, D., Annabi-Bergaya, F., Yan, W., Liu, D., Liu, Z., 2013. From platy kaolinite to aluminosilicate nanoroll via one-step delamination of kaolinite: effect of the temperature of intercalation. Appl. Clay Sci. 83–84, 68–76.

Yuan, P., Tan, D., Annabi-Bergaya, F., 2015a. Properties and applications of halloysite nanotubes: recent research advances and future prospects. Appl. Clay Sci. 112, 75–93.

Yuan, W., Yuan, P., Liu, D., Yu, W., Deng, L., Chen, F., 2015b. Novel hierarchically porous nanocomposites of diatomite-based ceramic monoliths coated with silicalite-1 nanoparticles for benzene adsorption. Microporous Mesoporous Mater. 206, 184–193.

Yuan, P., Thill, A., Bergaya, F., 2016. Nanosized Tubular Clay Minerals. Elsevier, Amsterdam.

Zhang, A.-B., Pan, L., Zhang, H.-Y., Liu, S.-T., Ye, Y., Xia, M.-S., Chen, X.-G., 2012a. Effects of acid treatment on the physico-chemical and pore characteristics of halloysite. Colloid Surf. A 396, 182–188.

Zhang, Y., Fu, L., Yang, H., 2012b. Insights into the physicochemical aspects from natural halloysite to silica nanotubes. Colloid Surf. A 414, 115–119.

Zhao, X., Ma, Q., Lu, G., 1998. VOC removal: comparison of MCM-41 with hydrophobic zeolites and activated carbon. Energy Fuel 12, 1051–1054.

Zhong, Y., Liang, X., He, Z., Tan, W., Zhu, J., Yuan, P., Zhu, R., He, H., 2014. The constraints of transition metal substitutions (Ti, Cr, Mn, Co and Ni) in magnetite on its catalytic activity in heterogeneous Fenton and UV/Fenton reaction: from the perspective of hydroxyl radical generation. Appl. Catal. B Environ. 150, 612–618.